ChemElectroChem

Research Article
doi.org/10.1002/celc.202300725

Chemistry Europe
European Chemical Societies Publishing

www.chemelectrochem.org

Transforming Cigarette Wastes into Oxygen Reduction Reaction Electrocatalyst: Does Each Component Behave Differently? An Experimental Evaluation

Giovanni Zuccante,[a, b] Mohsin Muhyuddin,[a] Valerio C. A. Ficca,[c, d] Ernesto Placidi,[d] Maurizio Acciarri,[a] Niccolò Lamanna,[e] Andrea Franzetti,[e] Luca Zoia,[e] Marco Bellini,[f] Enrico Berretti,[f] Alessandro Lavacchi,[f] and Carlo Santoro*[a]

Trillion of cigarette butts are annually littered without being recycled. This work aims at valorizing the whole cigarette butts and their components (paper, filter and tobacco) into Fe-N_x-C electrocatalysts for oxygen reduction reaction (ORR) in acid and alkaline media. The pristine wastes were pyrolyzed at 450 °C, activated with KOH at 700 °C, blended with iron phthalocyanine (FePc) precursor, and heat-treated at 600 °C to produce a robust Fe-N_x-C material with ORR active units. The effect of the cigarette components on the final electrocatalytic activity was evaluated by thoroughly investigating the surface chemistry with XPS. The electrocatalysts displayed similar results among the different components in both media due to comparable surface chemistry, especially concerning the nitrogen functional groups. The highest performance was obtained in alkaline where the electrocatalysts from whole cigarettes and paper (CIGF_450 and CIGPF_450) showed an $E_{1/2}$ of 0.89 V vs RHE, slightly larger than that of Pt/C with 40 wt% of Pt, which encouraged to replace Pt-based electrocatalysts in alkaline fuel cells.

Introduction

Low-temperature fuel cells (FCs) are evolving as promising sustainable devices in the paramount of clean energy production due to their exceptional advantages.[1,2] Among the cutting-edge FCs, proton exchange membrane FCs (PEMFCs) and anion exchange membrane FCs (AEMFCs) have appealed interest of researchers owing to their technological advancements and potential for mobile and stationary applications.[3–5] Both devices can easily convert the fuel (hydrogen) into water as an environment-friendly product in different pH environments by exploiting the combined action of hydrogen oxidation reaction (HOR) at the anode and the oxygen reduction reaction (ORR) at the cathode.[6] Although these bleeding-edge technologies are gaining relatively high business prosperity, the complex and slow-paced ORR hinders their implementation in far-reaching applications. According to the scientific community, ORR can mainly proceed via two pathways, *i.e.* the tetra-electronic and the bi-electronic.[7] The former is the most desired route since it leads to water or OH^- as a final output depending on the pH. In contrast, the latter brings aggressive peroxide species, which can severely damage the membrane integrity and consequently decrease the whole FC performance.[8] To overcome these issues, platinum group metals (PGMs) are widely employed in FC cathodes.[9,10] However, this practice soars the fuel cell stack cost making FCs less competitive than fossil fuel-based technology in the energy production market.[11] Therefore, scientists are putting strong efforts into making FC technologies economically viable by developing efficient and cost-effective carbon-based electrocatalysts to replace PGMs.[10,12–17]

Carbon-based nanomaterials are known to provide conductive and robust support for the electrocatalytic activities in FCs,[81–83] however, they are typically derived from the petrochemical industries.[18] The basic demand to reduce production costs and efficiently use resources drives us to follow the circular economy principles of recycling the ever-increasing organic waste which is otherwise a persistent challenge to the environment's safety. Biomass and plastic-based scraps are emerging as possible carbon feedstock to produce active materials for catalyst and electrode applications since these

[a] G. Zuccante, M. Muhyuddin, Prof. M. Acciarri, Prof. C. Santoro
Electrocatalysis and Bioelectrocatalysis Lab, Department of Materials Science, University of Milano-Bicocca, U5, Via Cozzi 5, 20125, Milano, Italy
E-mail: carlo.santoro@unimib.it

[b] G. Zuccante
Department of Industrial Engineering, University of Padova, Via Marzolo 9, Padova, 35131, Italy

[c] Dr. V. C. A. Ficca
Department of Chemistry, Sapienza University of Rome, Piazzale Aldo Moro 5, 00185 Rome, Italy

[d] Dr. V. C. A. Ficca, Prof. E. Placidi
Department of Physics, Sapienza University of Rome, Piazzale Aldo Moro 2, 00185 Roma, Italy

[e] N. Lamanna, Dr. A. Franzetti, Prof. L. Zoia
Department of Earth and Environmental Sciences, University of Milano-Bicocca, Building U01, Piazza della Scienza 1, 20126 Milan, Italy

[f] Dr. M. Bellini, Dr. E. Berretti, Dr. A. Lavacchi
Istituto di Chimica Dei Composti OrganoMetallici (ICCOM), Consiglio Nazionale Delle Ricerche (CNR),
Via Madonna Del Piano 10, 50019 Sesto Fiorentino, Italy

Supporting information for this article is available on the WWW under https://doi.org/10.1002/celc.202300725

sources can be easily converted into porous and conductive carbonaceous chars through pyrolysis.[19,20] Among the various sorts of difficult-to-manage wastes that fall outside the traditional recycling pathways, discarded cigarette butts (CBs) are the challenging ones that are littered in common waste streams with up to 6 trillion per year.[24,25] Their ubiquitous dispersion results in a final release of 300,000 tons of microplastic from the 60 filters as well as more than 7,000 hazardous ingredients[26,27] where a single CB can contaminate up to 1000 L of water.[28,29] Hence, to avoid such terrible effects and promote a circular economy paradigm their upcycling into value-added products for sustainable applications should be encouraged and one of the potential ways could be their transformation into electrocatalysts for ORR which is the key bottleneck in the commercial realization of FCs.

In the arena of carbon-based nanomaterials, metal-nitrogen-carbons (M–N–Cs) are gaining the attention of the scientific community as the most reliable replacement for PGMs. Such M–N–Cs are based on the atomic level dispersion of first-row transition metals (TM) in a nitrogen-doped porous and defect-rich matrix of carbon.[30] TM with atomic level coordination with nitrogen i.e. TM–N4, TM–N3, TM–N2[30–32] makes robust active moieties for the direct tetra-electronic ORR. Whereas the metal-free nitrogen-based active sites such as pyrrolic and pyridinic help in the bi-electronic and 2 + 2 stepwise reduction of oxygen during the electrocatalysis.[33,34] Compared to the other choices of TMs, Fe comes first owing to the optimum electronic structure that facilitates the cleavage of O=O while promoting the direct 4-electron pathway.[35] Hence, Fe–N–Cs have evolved as an important PGM alternative for ORR. It is important to note that Fe–N–Cs and other TM-based electrocatalysts are majorly composed of carbon and this carbon can be cost-effectively synthesized using waste plastic and biomass. Therefore, a huge academic interest has recently been witnessed in the utilization of plastics and biomass waste.[13,36–38] Recently, different waste materials such as polyethylene terephthalate (PET) packaging[39] and bottles,[40] facemasks,[36] polypropylene lunchboxes,[23] waste tires,[37] polyurethane,[13] pistachio shells,[41] waste tea,[42] waste leather,[43] spent batteries,[44] several bio-based waste[45–47] and so on have been utilized as a carbon feedstock to develop PGM-free catalysts i.e. Fe–N–Cs for ORR via pyrolysis. With the same pursuit, recently, our research group attempted to synthesize Fe-N_x-Cs catalysts for ORR starting from cigarette butts[48] optimizing the synthesis process in two-step pyrolysis at 450 °C and 600 °C, with an intermediate activation process to increase the surface area. The obtained materials resulted in selective oxygen conversion throughout the 4-electron pathway.[48] Despite the initial encouraging outcomes of the Fe–N–Cs synthesis using waste CBs, important queries still must be resolved. Discarded CBs are composed of various parts having different chemistry and elemental nature. Therefore, commencing an inclusive analysis of their utilization in Fe–N–Cs production is critical, as different feedstocks can rigorously influence the final characteristics of the derived catalysts. This is particularly important while designing single-atom catalysts (SACs) i.e. Fe–N–Cs, where even a slight modification in the proportion of ingredients and impurities can lead to varied consequences.

In this paper, we aim at investigating the effect of using different components of cigarette butts as carbon precursors, *i.e.* tobacco, rolled paper, and filter on the ORR electrocatalytic activity. Since these components are prepared in a different way and designed for different scopes, they display diverse chemical composition and morphology.[49] For instance, tobacco is a ligneous-cellulosic material containing a higher amount of metals and nitrogen than the cigarette filter, which is made of cellulose acetate and serves as a barrier preventing the entrance of noxious substances into the lungs.[50] The same consideration can be made for cigarette paper, which is a cellulose-based material and contains additives to improve the cigarette combustion process upon smoking.[51] All of these features are expected to play a role in the development of diverse carbonaceous structures during pyrolysis. Therefore, each cigarette component was pyrolyzed at the same optimal temperature, *i.e.* 450 °C, and subsequently activated and functionalized with FePc according to the previously used protocol.[48] The electrochemical results were achieved via RRDE and compared with the carbon obtained by pyrolyzing the whole cigarettes in both acid and alkaline media.

Results and Discussion

Figure 1 illustrates the main steps of the electrocatalyst preparation, *i.e.* the pyrolysis to convert the waste CBs into carbonaceous char, the KOH activation to expand the pore network, and finally the functionalization to launch the active sites. Regarding the preparation of carbon materials, the output gravimetric yield of pyrolysis (calculated as described in the Experimental Section) represents an essential parameter affecting the decision-making process of industrial scalability. All three materials show three different yields as reported in Table S1 in Supplementary Information. The highest one (*ca.* 40 %) was obtained by tobacco, while the lowest one (ca. 20 %) was reached by filter. Whole cigarettes and paper achieved intermediate values of 26 % and 36 %, respectively. Similar results were obtained by S. Yousef *et al.*, who observed a greater degradation for the filter with respect to the other cigarette components.[52]

Morphological and Chemical Analysis

The surface morphology of the final electrocatalysts is compared with that of the pristine materials, *i.e.* filter, paper, and tobacco, in Figure S1 and Figure S2 within Supplementary Information. The texture of the final materials (Figure S1), which were ground into fine powders, looks similar and it is mainly characterized by aggregated, globular, and irregularly shaped microparticles, similar to cigarette-derived carbon reported in other works.[53] The pristine materials exhibit a distinguishable texture from each other (Figure S2). In Figure S2a, the particles of tobacco powder possess a rough, and carved surface typical

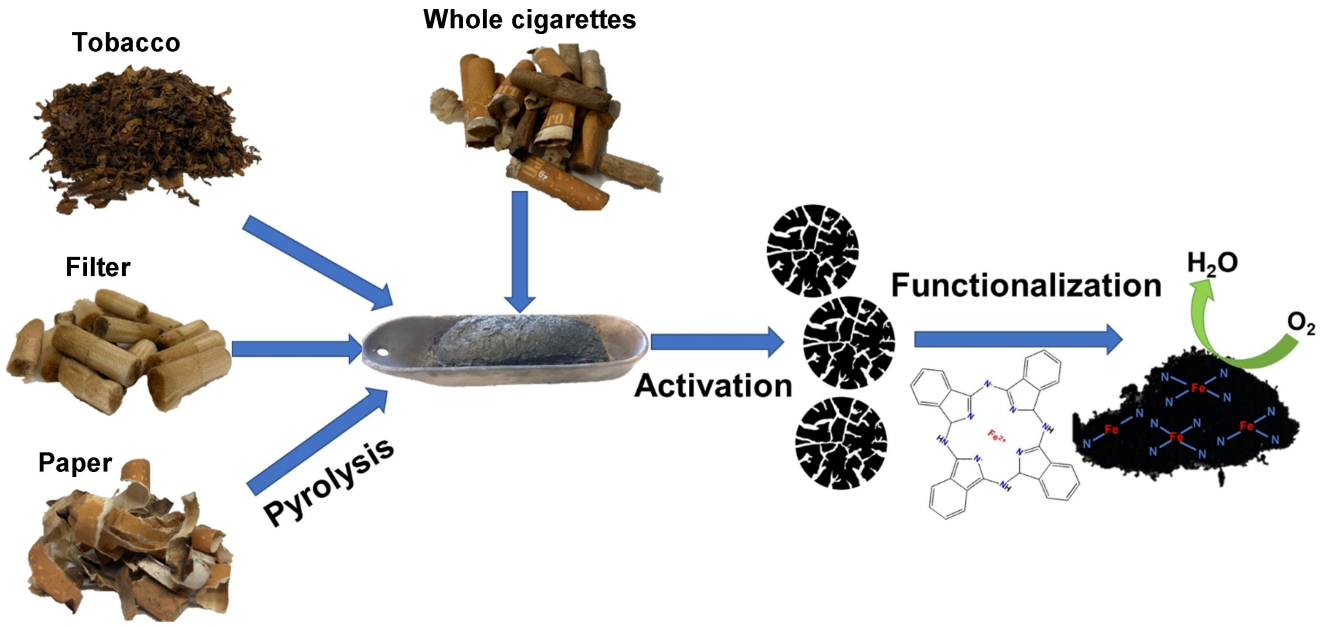

Figure 1. Sketch of the electrocatalyst preparation.

of lignocellulosic biomass materials with some cavities.[54] On the contrary, the paper shows a smoother surface than tobacco with some cracks (Figure S2b). Eventually, the filter is composed of Y-shaped long fibers having a diameter of *ca.* 20 micrometers and a length probably over several hundred micrometers (Figure S2c).[55,56]

The quantification of carbon, nitrogen, and hydrogen of the pristine material and the prepared electrocatalysts is depicted in Table S2, where the results are reported in wt%. At first glance, the electrocatalyst material presents a high amount of carbon compared to the raw material (*ca.* 42.68 wt% on average vs 74.46 wt% on average) while hydrogen content is higher for the waste source (*ca.* 5 wt% on average vs 1.6 wt% on average). The increase of carbon and the decrease of hydrogen content is attributed to the pyrolysis performed at 450 °C and the following thermal treatment performed at higher temperatures, where H is removed through the elimination of water molecules and volatile aromatic compounds (*e.g.* phenols).[52] In the pristine material, the quantity of nitrogen is below 1 wt% in the case of cigarette, paper, and filter while it is more than 2 wt% in the case of tobacco. Such a high amount in tobacco is due to the presence of numerous N-containing molecules, including aromatic nitrosamines (*e.g.* nicotine) and hydrogen cyanide.[57] In general, iron phthalocyanine precursor increases the amount of nitrogen so that the electrocatalysts display a higher content. Among the final materials, CIGTF_450 presents the greatest amount of N (i.e. 3.82 wt%), which might be due to the abundance of N inherited by the raw material, *i.e.* tobacco.

The occurrence of the main elements in both the pristine materials and the final electrocatalysts was determined by XRF spectroscopy and the resultant spectra are reported in Figure S3 and Figure S4, respectively. Ca, Fe, K, Ti, and Cr are the prevalent metallic elements in the pristine materials (Figure S3), with less sharp signals in the filter (Figure S3b). These elements come from additives introduced in cigarette components for different purposes. For instance, Ti derives from the introduction of TiO_2 as a whitening agent in the paper or to reduce the luster among the filter fibers,[49,58] while Ca and K from $CaCO_3$ and potassium carboxylates are added as flame retardants.[58–60] The presence of Fe in the pristine materials is justified by the addition of iron oxide additives as catalysts to convert CO into CO_2,[51] whereas the occurrence of Cr can have multiple origins, including the fertilizers used for tobacco cultivation.[61] Anyway, in the XRF of the final electrocatalysts (Figure S4), Fe results to be almost the only metal, obviously derived from FePc precursor whereas most of the aforementioned impurities do not appear in the final electrocatalysts, probably due to the acid washing, which leached out many metals found in the pristine materials.

To further analyze the morphological aspects of the derived electrocatalyst, transmission electron microscope (TEM) images were acquired as demonstrated in Figure 2. From TEM images it can be witnessed that the architecture of all the developed catalysts is mainly composed of amorphous carbon, with few defect-rich graphitic domains. The topography of the CIGF_450 was observed to be relatively rougher indicating the presence of structural discontinuities and edge defects. Moreover, all the samples exhibited tiny metallic nanoparticles wrapped within the few graphitic layers. Such morphological features were additionally confirmed by accruing the morphological and compositional contrasts through HAADF (High-Angle Annular Dark Field)-STEM (scanning TEM) and corresponding EDX area mappings (Figure S5). The STEM analysis certifies the homogeneous distribution of the elements of interest i.e. Fe and O throughout the carbon matrix of the derived catalysts, however, the coalescence of Fe species into nanoparticles is also quite evident. From the (Energy-dispersive X-ray spectroscopy) EDX

Research Article
doi.org/10.1002/celc.202300725
Chemistry Europe
European Chemical Societies Publishing

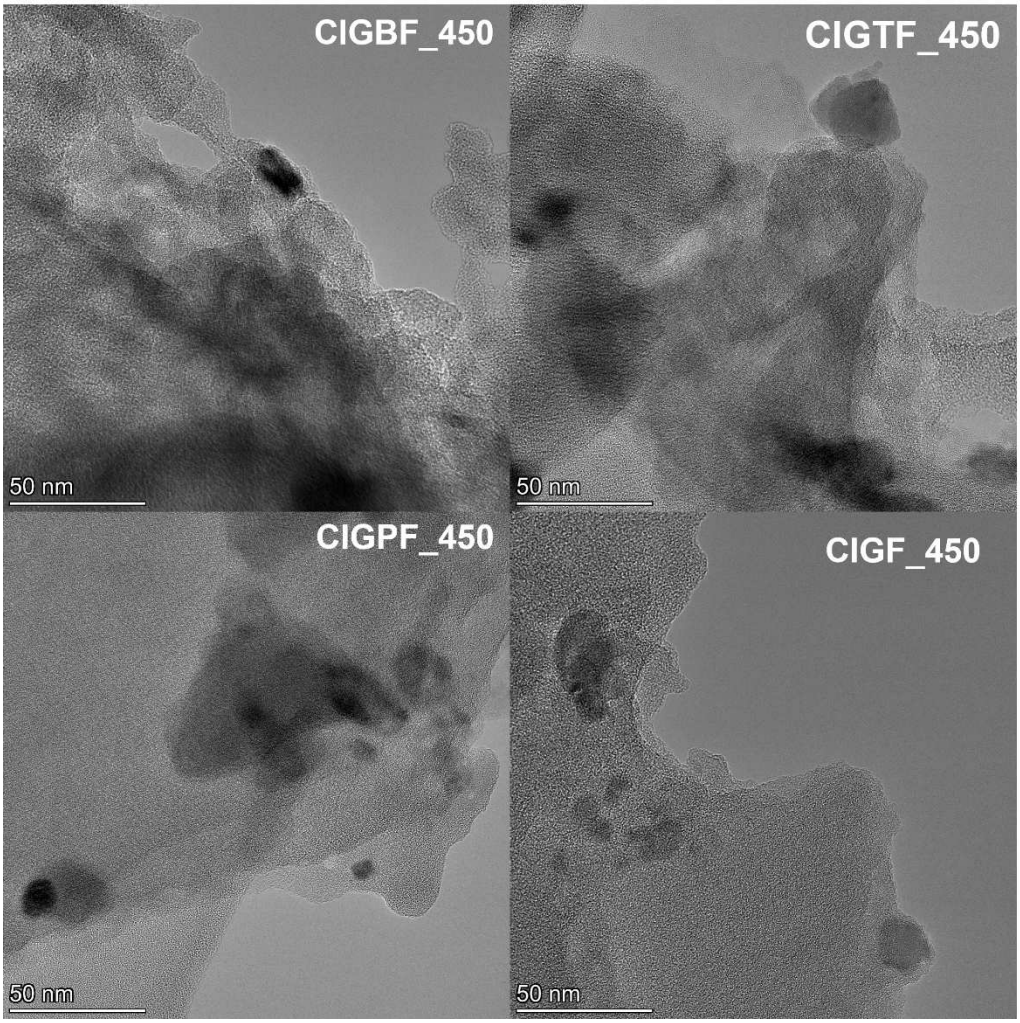

Figure 2. TEM micrographs of the derived electrocatalysts.

area maps it can be inferred that the Fe nanoparticles are mostly in the oxide forms.

The crystallography of the electrocatalyst was studied by XRD, and the diffractograms were reported below in Figure 3a. All the samples show broad peaks centered at *ca.* 26° and 44°

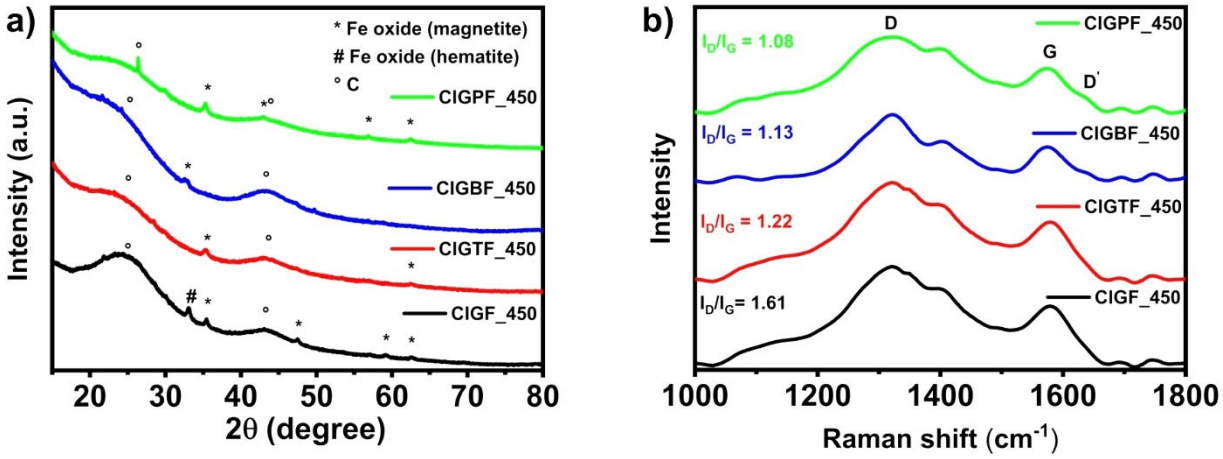

Figure 3. a) XRD and b) Raman spectra of the electrocatalysts.

ascribed to amorphous carbon and resulting from the crystallographic planes (200) and (110) of graphite (ICDD: 01-089-7213).[62] As well as carbon peaks, all the XRD patterns depict tiny peaks at *ca.* 32.5, 35.3, 47.6, 56.84° arising from iron oxide with mixed Fe(II), Fe(III) oxidation state (*i.e.* Fe_3O_4 magnetite, ICDD: 01-086-1356), but the peak at 33° in ClGF_450 evidence the presence of hematite phase (Fe_2O_3, ICDD: 01-085-0987). Hence, from the crystallographic point of view, the materials seem to be composed of a few iron oxide crystallites dispersed in an amorphous carbon matrix. The indication of iron oxide presence is supported by the afore-discussed STEM and EDX analysis.

As a non-destructive technique, Raman spectroscopy was carried out to gain insights into carbon structure, and the corresponding spectra are reported in Figure 3b. The as-prepared electrocatalysts displayed the two usual signals of electroactive carbon materials in the first-order spectra, *i.e.* the G and D bands. In the prepared electrocatalysts, the former is located at roughly 1575 cm^{-1} and it derives from the E_{2g} mode of the in-plane sp^2 bond-stretching of C atoms whereas the latter is centered at *ca.* 1320 cm^{-1} and emerges from the A_{1g} breathing mode of C–C around defects.[63,64] Looking closer, the D′ (also known as D2) peak appears as a shoulder of the G band at *ca.* 1630 cm^{-1}, especially for ClGPF_450 and ClGBF_450. Even this band is associated with a defective structure[65] but, more specifically, refers to lattice vibration involving graphene layers at the surface of a graphitic crystal, namely those layers not directly sandwiched between two other graphene layers.[66] The I_D/I_G ratio, which is related to carbon defectivity, was calculated by dividing the absolute intensity of the D band and that of the G rather than the peak area because the herein synthesized materials are amorphous and present a high defect density.[67] Indeed, the I_D/I_G ratio is higher than 1 and spans between 1.08 of ClGPF_450 and 1.61 of ClGF_450. The higher defect density of the ClGF_450 revealed by Raman spectra further endorses the TEM outcomes. Also, XRD patterns exhibited amorphous carbon humps at *ca.* 26° and 44° clearly confirming the defective carbonaceous matrix that could help in ORR activity.[68,69] The other two samples, *i.e.* ClGBF_450 and ClGTF_450, exhibit intermediate values, *i.e.* 1.13 and 1.22 respectively. Hence, such high I_D/I_G and the appearance of D′ shoulder confirm the occurrence of a large number of defects, such as heteroatom substitutions, destructive grain boundaries and edges due to micropore formation or the presence of iron oxide phases (as detected in XRD), atomic vacancies, cracks, etc.[67]

To analyze the textural characteristics of the developed samples, BET analysis was performed. The results of the obtained adsorption-desorption curves have been displayed in Figure S6 whilst Table S3 summarizes the BET results. The shapes of obtained isotherms with a high uptake at low relative pressures typically indicate the presence of microporous systems. Moreover, the high surface area, in conjunction with the small pore width calculated with the BJH method suggests heterogeneous porosity of the samples, where macro and mesopore coexist. ClGBF_450 adsorption-desorption isotherm shows an H4 hysteresis, typical of narrow-slit pores. These pores can be represented as the gaps between the layers of a lamellar packaged material. It is worth noting that ClGPF_450 showed a remarkable surface area of 1715.98 $m^2 g^{-1}$ whereas the surface area of ClGTF_450 and ClGF_450 came out to be 1057.50 $m^2 g^{-1}$ and 932.18 $m^2 g^{-1}$, respectively. However, ClGBF showed the least surface area of 649 $m^2 g^{-1}$ with a minimum BJH desorption cumulative pores volume. It is important to underline that accessibility to the active sites is an essential prerequisite because if the active sites are present but remain inaccessible, they cannot contribute to the ORR. Therefore, higher surface area and meso-macroporous architecture ensure adequate accessibility to the active sites and mass transportation.

Next, the four samples based on cigarette butts were characterized by means of XPS to investigate the surface chemistry, which plays a pivotal role in the electrocatalytic performance of carbon-based materials. The wide scans, reported in Figure S7, are comparable among the samples and identified four elements in decreasing amounts, respectively C1s, O1s, N1s, and Fe2p. Table S4 summarizes the elemental composition in at%, which is predominantly carbon, with an average of 6.6 at% of oxygen, 5.4 at% of nitrogen, and around 0.56 at% of iron. Specifically, the C content decreased in the order ClGF_450 > ClGBF_450 > ClGPF_450 > ClGTF_450, while the opposite trend was found for the nitrogen. Regarding Fe, ClGF_450 resulted in the lowest content with just 0.34 at.% while ClGPF_450 had the highest (0.69 at%), almost double compared to the reference sample. For each sample the identified core levels' spectra were fitted according to previous studies,[70–75] the results of which are reported in Figures S8 (C1s), Figure 4 (N1s), and Figure S9 (O1s), Figure 5 (Fe 2p) and summarized in Table S5.

The C1s, N1s, O1s, and Fe2p spectra were very similar among the samples with lesser modifications in the shape; sample ClGF_450 showed slightly broader N1s (Figure 4a) with respect to the others impacting the amount of N moieties. The carbon content was found to be predominantly sp^2 graphitic (284.5 eV), with an average above 50 rel%, followed by defective structures located below 284 eV accounting for 10.8 rel%. The third main component is the disordered sp^3 C (~285.1 eV), in an amount comparable to defective C. The sample ClGPF_450 resulted in the lowest sp^2 C content whilst ClGTF_450 possesses the highest (Table S5). In Figure S8, the appearance of minor peaks at 285.8, 287, 288 and 290 eV assigned to C–N, C–OH/C–O–C, C=O/O–C–O, and COOH witness a variety of functional groups on the graphitic basal plane, which can locally tune the carbon conductivity.[76] Indeed, the abundance of sp^2 carbon (C=C) arising from the disordered carbon graphitic lattice is vital for electronic conductivity as much as the presence of electron-donating atoms, like nitrogen.[77]

Regarding nitrogen, the XPS deconvoluted spectra are reported in Figure 5. The deconvolution shows the appearance of six different N-moieties: imine (~398 eV), pyridinic-N (~398.5 eV), N_x-Fe (~400.0 eV), pyrrolic-N (~400.8 eV), graphitic-N (~402 eV) and oxidized nitrogen species NO_x (~404 eV). The main component was identified as pyridinic N, located at ~398.5 eV (~50 rel%), which increases according to this trend: ClGF_450 < ClGBF_450 < ClGPF_450 < ClGTF_450. The second

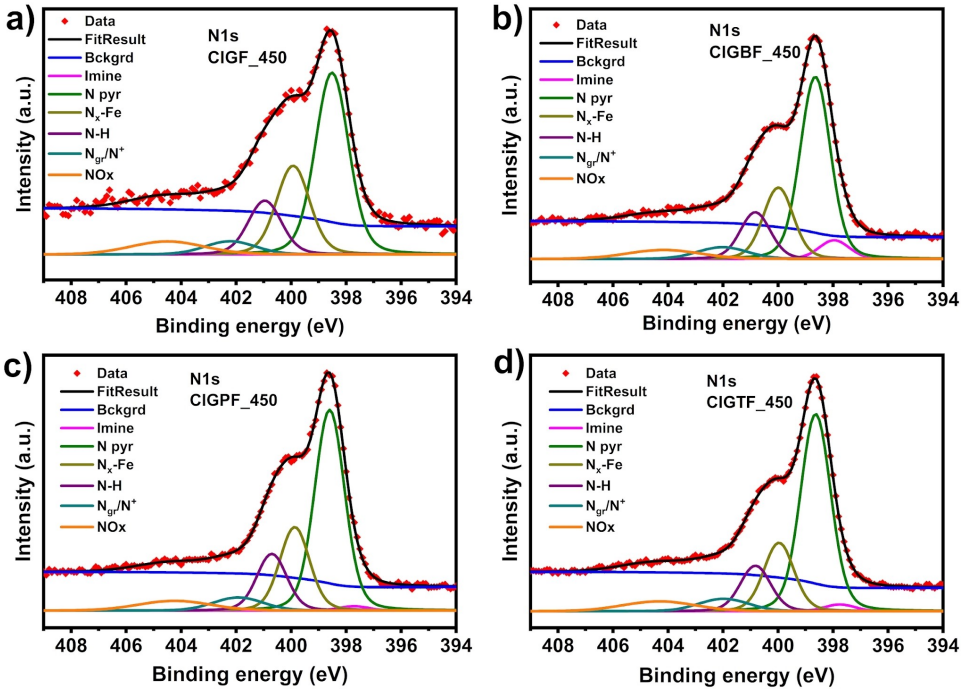

Figure 4. N1s high resolution spectra of the electrocatalysts.

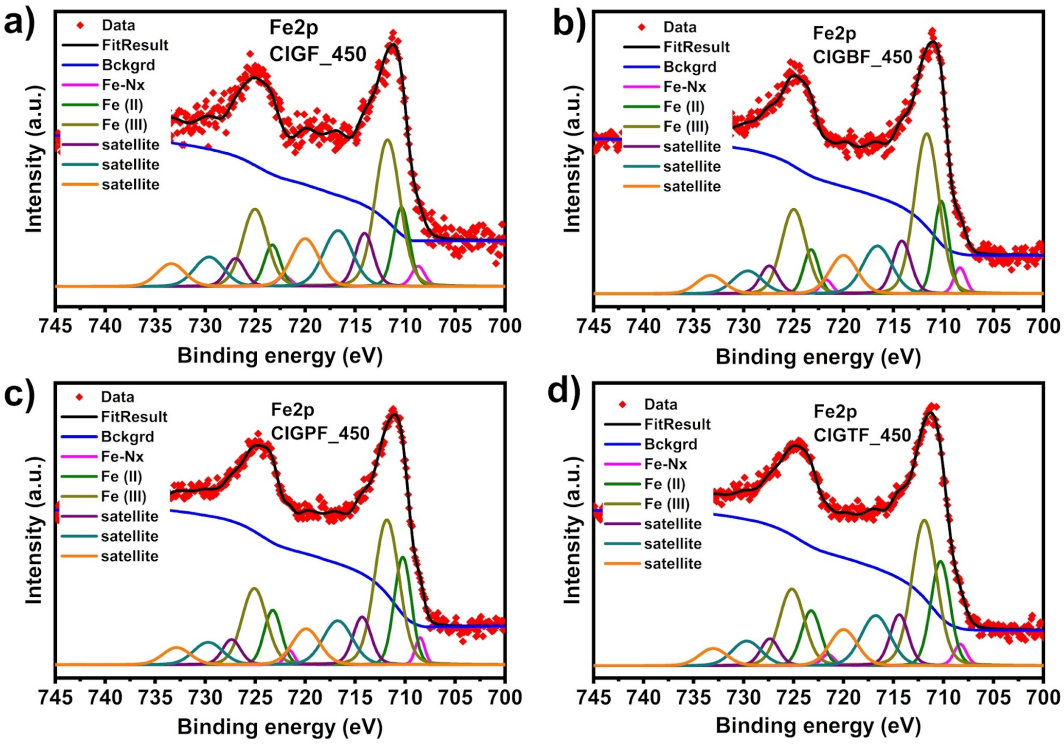

Figure 5. Fe2p high-resolution spectra of the electrocatalysts.

important component was the nitrogen coordinating the iron (N_x-Fe, ~399.9 eV), followed by pyrrolic-N (~400.9 eV). Comparing the samples, CIGF_450 was found to have the highest amount of N_x-Fe (23.9 rel %) while CIGTF_450 possesses the lowest (19 rel %). N_x-Fe takes a leadership role in ORR, catalyzing the production of water or OH^- either through the direct 4-electron pathway or the indirect 2×2-electron pathway,[30] which occurs via the production of peroxide at the first reduction step (upper potentials), and water or OH^- at the second reduction step (lower potentials).[78] Metal-free N-moieties where N is

hybridized in sp^3 form, such as graphitic-N and pyrrolic-N, are supposed to catalyze the 2-electron pathway according to previous reports.[33,79] However, other researchers argue that pyrrolic-N can address the 4-electron pathway.[80] Moreover, graphitic-N can have a positive influence on proton transfer during the ORR mechanism in the acid environment.[77] The sp^2 N-moieties like the pyridinic-N are likely to promote the reduction of peroxide into the final product, *i.e.* water or OH^-.[77,81]

Moving on to oxygen, the O1s high-resolution spectra, reported in Figure S9, were deconvoluted in 4 peaks centered at 530, 531, 532, 533 eV corresponding to Mox, M–OH/C=O, C–OH/C–O–C, O–C–O, respectively. The appearance of Mox and M–OH signals confirms that oxygen is not only bonded to carbon but also to iron, corroborating the existence of iron oxide phases shown in XRD spectra. While the role of nitrogen moieties in ORR is widely discussed in literature, the function of oxygenated groups is not highly debated. Only a few articles report the positive influence of oxygen-functional groups on ORR such as C–OOH and C=O in conductive carbon supports but further studies are needed to support this statement.[82]

Finally, the Fe2p shape of spectra is compatible with systems obtained from Fe(II) compounds[83] containing both Fe(II) and Fe(III) in high-spin state due to the presence of multiplets and satellites, broadening the $2p_{3/2}$ component,[84] as shown in Figure 5. The prominence of Fe(III) can be ascribable to air exposure of samples, where oxygen can easily bind to the Fe(II) sites of Fe-N_x centers. Also, some Fe(III) species can be embedded in the few crystallites magnetite or hematite phases together with Fe(II), which were detected by XRD and probably enucleated during the heat treatment.[48] About the Fe moieties, the majority of surface iron was in the oxidation state +3 (~711.8 eV), about 70 rel% for ClGF_450 and ClGBF_450, 63.6 rel% for ClGPF_450 and 61.7 rel% for ClGTF_450, the latter possessing also the highest content of Fe(II) (~710.3 eV), about 33.5 rel%. The N-coordinated Fe was also identified in a similar amount for all samples (*ca.* 5 rel%) and no metallic phases were found, which corroborates the atomically dispersed nature of iron.[85]

Electrochemical Measurements

To assess the electrocatalytic activity of the synthesized electrocatalysts towards ORR, RRDE measurements were carried out in 0.5 M H_2SO_4 acidic and 0.1 M KOH alkaline electrolyte. Hence, linear sweep voltammetry (LSV) curves of the disk (J_{disk}) and ring current densities (J_{ring}) were acquired under a rotation speed of 1600 rpm and 5 mV/s, as conventional parameters to compare different electrocatalysts in literature.[86,87] Onset potential (E_{on}) and half-wave potential ($E_{1/2}$) were calculated from J_{disk} curve as kinetic indicators to compare the electroactivity of the different materials. As a threshold potential to start the ORR, E_{on} was determined around – 0.1 mA cm^{-2} while $E_{1/2}$ was determined at the maximum of the first derivative, according to previous ORR protocols. Furthermore, the limited current (J_{lim}), *i.e.* the maximum current value reached when the electrochemical process is controlled by diffusion of reactant species, can be utilized as a further parameter to discriminate the performance of electrocatalysts with comparable E_{on} and $E_{1/2}$. As well as electroactivity, the selectivity towards the 4-electron pathway is another essential feature to consider, especially when the electrocatalysts are designed for PEMFCs since the PEM membrane cannot withstand the aggressive action of peroxide species.[88] The peroxide production was given by equation (4.1), which includes the contribution of both J_{disk} and J_{ring} whereas the number of transferred electrons n was calculated by eq. (4.2). It was witnessed that the enhancement of the derived electrocatalysts is solely attributed to the activation and functionalization of the char-acquired during the first pyrolysis (refer to Figure S10 and Figure S11 in the supplementary information with due explanation).

Acidic Electrolyte

The evaluation of RRDE electrocatalytic activity in an acid electrolyte at pH near 0 is extremely important to gain a first insight into the potential application of TM-Nx-C electrocatalyst in the almost mature PEMFC technology.[89] As preliminary results for the ORR activity evaluation, cyclic voltammetries were performed at 5 mV s^{-1} without rotation on each sample and reported in Figure S12. The appearance of a faradic peak at ca. 0.7 V vs RHE (reported in Table S6) in ClGF_450, ClGTF_450 and ClGPF_450 indicates an ORR activity for these electrocatalysts. The same peak is however missing in the ClGBF_450 voltammogram, suggesting limited performance compared to the other electrocatalysts. Figures 6a and 6b active sites the results for disk and ring current density recorded in O_2 saturated electrolyte, respectively, whereas Figures 6c and 6d show the peroxide % and the number of transferred electrons (n), respectively. Apart from ClGF_450, which reaches a J_{lim} of – 2.7 mA cm^{-2} at potentials lower than 0.3 V vs RHE, the other electrocatalysts do not reach the diffusion-limiting current in the measured potential window. For these electrocatalysts the current plunges between 0.7 and 0.6 V vs RHE, where the process is controlled by only kinetics. However, at a potential lower than 0.5 V vs RHE, the J_{disk} curve steadily decreases, meaning that the electrochemical process is still controlled by both mass transfer and kinetics. The $E_{1/2}$ and E_{on} show similar values among the electrocatalysts as they span within a narrow range of 0.61–0.64 and 0.75–0.78 V vs RHE, respectively. However, it should be evidenced that ClGBF_450 develops a much lower current at equal potential compared to the other electrocatalysts. It should be noted that the same sample exhibited the least surface area and the inaccessibility of the active sites might be the possible reason for this discrepancy. For instance, the difference of current detected at 0 V vs RHE is *ca.* 0.5 mA cm^{-2} than that of the other electrocatalysts. Similarly, to the J_{disk} trend, the J_{ring} achieved at 0 V vs RHE by ClGBF_450 is much lower compared to that recorded for the other electrocatalysts, *i.e.* 0.075 vs 0.12 mA cm^{-2}. Combining the J_{disk} and J_{ring} results in the equation (4.1), the peroxide production was determined and the trend is reported in Figure 6c. All in all,

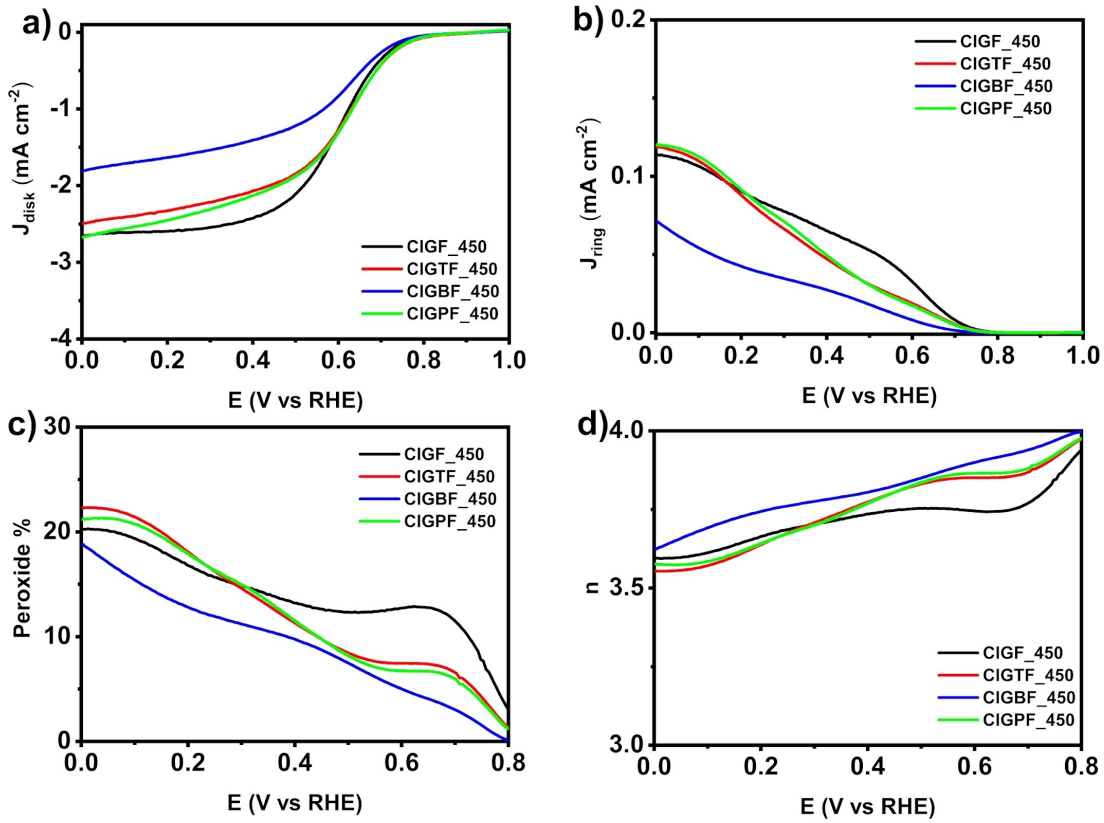

Figure 6. Electrochemical results in 0.5 M H_2SO_4 electrolyte at 1600 rpm and 5 mV s^{-1}: a) disk current, b) ring current, c) peroxide %, and d) number of transferred electrons.

the electrocatalysts achieve similar values of hydrogen peroxide production at 0 V vs RHE covering the interval 19–22%, with the lowest number for CIGBF_450. These outcomes reflect on the number of transferred electrons reaching *ca.* 3.6, with a slightly higher value for CIGBF_450 (*ca.* 3.7). Being these numbers close to 4, it is possible to ascertain the preferential water production pathway.

To elucidate the kinetics of the prepared electrocatalysts, Tafel analysis at low overpotential, i.e. between the E_{on} and $E_{1/2}$ was performed and the results are displayed in Figure S15a and in Table S7. The Tafel slope of the herein synthesized materials is quite similar, ranging between 117 and 121 mV dec^{-1}. This means that the electrocatalysts show similar kinetics.

Moreover, the operational durability of the best-performing electrocatalyst i.e. CIGTF_450 was analyzed in the acidic media which came out to be limited as the performance substantially decayed after 2000 cycles (Figure S13). It is well known that Fe–N–Cs are not very stable in the acidic medium and can be utilized to replace PGMs in the AEMFC where the higher pH environment can reduce the corrosion conditions.[90]

Alkaline Electrolyte

The ORR kinetics is more favored in the alkaline media than the acidic one and thus it is more promising for the fledgling TM–N–C materials. Some well-designed TM–N–C electrocatalysts can achieve or even exceed the performance of Pt/C. Thus, to ascertain the practicability of the performance of the as-synthesized Fe–N–C electrocatalysts was compared to that of 40 wt% Pt/C, which is one of the topmost ORR electrocatalysts. As preliminary results for the ORR activity evaluation, cyclic voltammetries were performed at 5 mV s^{-1} without rotation on each sample and reported in Figure S14. The presence of a reduction peak between 0.85–0.90 V vs RHE in all the electrocatalysts designates an ORR activity for these electrocatalysts.[91] After verifying the presence of an ORR activity, the analysis continues with LSV comparison obtained under rotation and illustrated in Figure 7a. A first look at Figure 7a shows a much lower overpotential compared to the acidic environment, with E_{on} approaching to 1 V vs RHE, and almost a perfect J_{disk} sigmoidal shape with the presence of limiting current plateau at a potential lower than 0.4 V vs RHE. As in the acidic environment, the electrocatalysts exhibit similar performance in the kinetic region with a narrow E_{on} and $E_{1/2}$ interval of ca. 20 mV, as shown in Table 1. The CIGPF_450 and CIGF_450 delivered the highest E_{on} and $E_{1/2}$ of ca. 0.94 V vs RHE and 0.89 V vs RHE, respectively. However, CIGF_450 exhibited higher J_{lim} than CIGPF_450 making it a slightly better candidate compared to CIGPF_450. On the other hand, although J_{lim} of CIGTF_450 came out to be maximum compared to other PGM-free counterparts, its minorly lower E_{on} and $E_{1/2}$ categories it as slightly less performing catalysts with relatively lower kinetics.

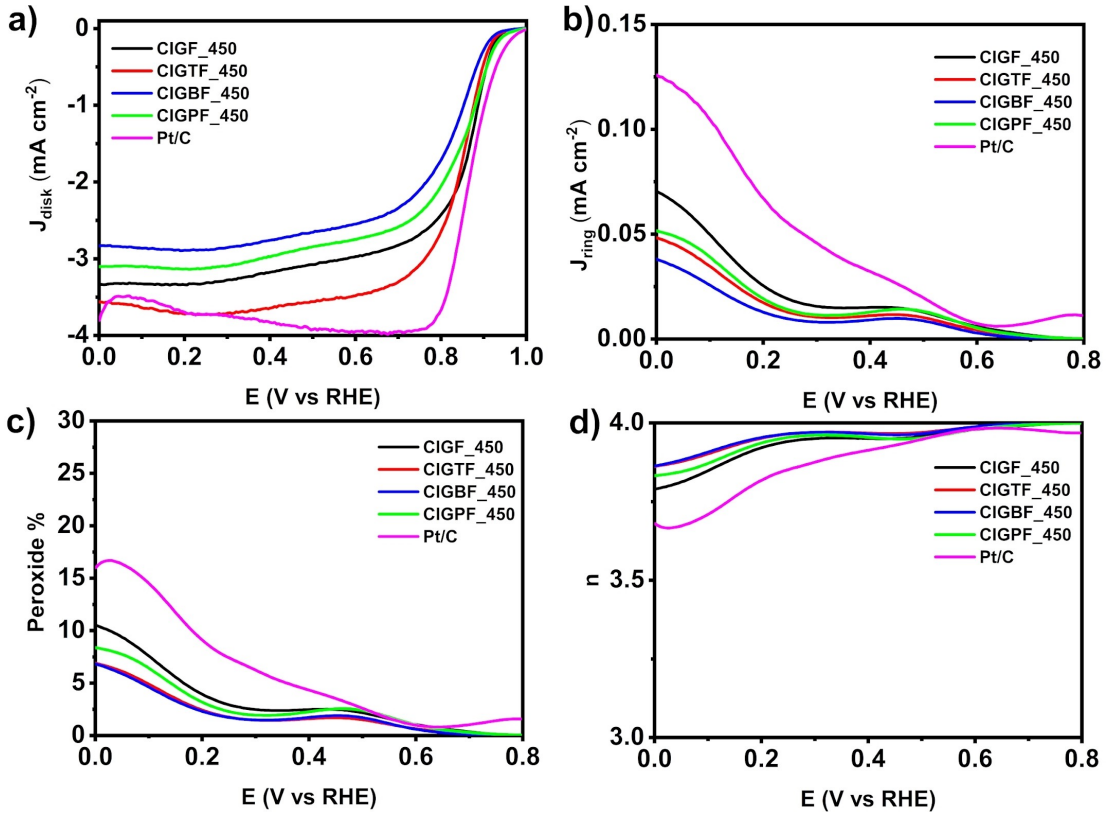

Figure 7. Electrochemical results in 0.1 M KOH electrolyte at 1600 rpm and 5 mV s^{-1}: a) disk current, b) ring current, c) peroxide %, and d) number of transferred electrons.

Table 1. Electrochemical results in acid and alkaline media.

	Acid		Alkaline	
	$E_{1/2}$	E_{on}	$E_{1/2}$	E_{on}
CIGF_450	0.61	0.76	0.89	0.94
CIGBF_450	0.64	0.75	0.87	0.92
CIGPF_450	0.63	0.77	0.89	0.95
CIGTF_450	0.64	0.78	0.87	0.93

In the given situation, among the tested electrocatalysts, CIGF_450 can be regarded as the optimum candidate owing to the best compromise between the E_{on} and $E_{1/2}$ parameters and the limiting current. However, the electrocatalysts fabricated by other cigarette components i.e. CIGTF_450 and CIGBF_450 also exhibited excellent ORR activity while remaining marginally lesser than that of CIGF_450, still ensuring their utility electrocatalysis. The extraordinary ORR kinetic parameters exhibited by the CIGF_450 can be attributed to higher structural defects as confirmed by XRD, Raman and TEM analysis along with the highest proportion of Fe-N_x moieties compared to the other samples. It is worth mentioning that Fe-N_x is the primary active site for the binding and then reduction of ORR while biomimicking the natural enzymes.[92] Moreover, the same sample illustrated reasonably good BET surface area with BJH desorption average pore width of 3.8 nm which was higher than the other samples and hence could provide a suitable scenario for the accessibility of the active sites while maintaining mass transportation. The significance of mesoporosity of narrow range is already known for enhanced ORR activity.[93,94] Moving to Pt/C comparison, the E_{on} of CIGF_450 is slightly below the 0.97 V vs RHE value achieved by Pt/C but the $E_{1/2}$ of all the as-synthesized electrocatalysts beats that of Pt/C (0.89 V vs RHE *vs* 0.86 V vs RHE). In Figure 7b, the J_{ring} current of the PGM-free electrocatalysts shows a sharp increase at potential $<$0.3 V vs RHE and a shoulder at 0.45 V vs RHE, maybe arising from water molecule reorientation and the redox conversion of quinone groups into hydroquinones, respectively.[95] As far as ORR selectivity is concerned, the production of peroxide of the as-synthesized electrocatalysts is almost below 10% and inferior to that of Pt/C, which arrives at 15% at 0 V vs RHE (Figure 7c). The lowest peroxide production of 7% is attained by CIGBF_450, whereas a slight increase in the peroxide yield was observed at a higher overpotential which might be due to the presence of graphitic and pyrrolic nitrogen known for increasing the peroxide. The peroxide yield affects the number of transferred electrons n (Figure 7d), which is very close to 4 (*i.e.* between 3.8 and 3.9 for the PGM-free and 3.7 for Pt/C), thus pointing out that the OH^- production is favored against the aggressive peroxide species.

As in the acid environment, the kinetics in alkaline of our electrocatalyst was studied via Tafel plots reported in Figure S15b and Table S7. At low overpotential, Pt/C standard shows a slope close to 60 mV dec^{-1}, according to previous

works,[96,97] and compatible with an oxide-covered surface, while the PGM-free materials herein examined exhibit a Tafel slope lower than Pt/C. These values are comparable to the most active Fe–N–C electrocatalysts found in the literature.[98]

To study the durability of the as-synthesized electrocatalyst RRDE stability test of 2000 cycles was performed only on ClGF_450 in 0.1 M KOH electrolyte since it is the best electrocatalyst, from our point of view. As depicted in Figure S16, the as-synthesized electrocatalyst shows excellent stability without any negative shift in the half-wave and onset potential, meaning that the kinetics is retained during cyclability. Small variations are observable in the peroxide production, which reaches *ca.* 7.5% at 0 V vs RHE at the beginning and rises to 9% after the 2000 cycles. This peroxide production change is also accompanied by a J_{lim} uplift of 1 mA cm^{-2} at 0 V vs RHE without negatively affecting the kinetic region. A drop in the electrocatalytic activity after 2000th cycle can be attributed to some sort of catalyst degradation. No doubt, Fe–N–C type catalysts display a great potential to substitute PGMs for ORR due to their optimum activity and cost-effectiveness, however, their inadequate operational durability could involve multiple and complicated degradation mechanisms which require in-depth investigations.[89,80,99,100] The most probable reason for the little decay in the performance could be Fe leaching from the nanoparticles and the poisoning of Fe-N_x sites due to hydroxyl species and generated peroxide.[101] Definitely, investigating the underlying degradation mechanism and then improving the operational stability of the active site structure is an essential requirement for the Fe–N–Cs, especially the waste derived but it remains outside the scope of the presented study. The clarification of this important aspect should be detailed and independently analyzed in the prospective research.

From the electrochemical point of view, the as-synthesized electrocatalysts show similar results among each other in both alkaline and acid media, confirming the utility of different parts of discarded cigarettes for catalyst fabrication. The amount of the Fe-N_x, metal-free nitrogen centers, which are the most considerable sites for the ORR mechanism, is quite similar among the electrocatalysts, although differences in the content of nitrogen and iron were detected. To mention differences, it should be pointed out that, in both media, it was observed that ClGBF_450 exhibited lower J_{lim} currents compared to the other electrocatalysts, which can be attributed to a lower exposition of the surface active sites on the material due to the lowest surface area confirmed by the BET analysis. Little dissimilarities observed in E_{on} and $E_{1/2}$ values among the electrocatalysts cannot be correlated with differences in surface chemistry. Considering E_{on} and $E_{1/2}$ and J_{lim} the results lead to the conclusion that ClGTF_450 is the most active electrocatalyst in acid environment while ClGF_450 beats all the other samples in alkaline media.

Noticeable differences in performance are instead observed by changing the electrolyte media. At high pH, the electrocatalysts show similar performance to Pt/C and the achieved results are comparable to the best electrocatalyst tested in other works under similar conditions.[102] The merit of such splendid achievements is due to the abundance of Fe-N_x and N-pyridinic moieties, which minimize the peroxide production and keep it lower than 10%, thus allowing for 4-electron catalysis. It is important to underline that ClGF_450 provides the optimum combination of higher structural defects, satisfactory surface area and higher proportion of Fe–Nx sites. Such attributes make ClGF_450 realize the best ORR performance, particularly in the alkaline media. The performance in terms of E_{on} and $E_{1/2}$ and J_{lim} are comparable to the best-performing biomass-based electrocatalysts synthesized in literature (Table S8). As far as iron oxide phases are concerned, there is no clear explanation of their influence on the ORR activity in alkaline. According to the majority of researchers, oxide phases are not electrochemically active sites or, in any case, they look less active than Fe-N_x sites.[103,104] Nevertheless, other studies claim that iron oxide nanoparticle encapsulation in carbon layers can uplift the ORR kinetics and, in some cases, endow structural robustness, thus preventing the corrosive dissolution of inactive metallic nanoparticles during ORR. However, in our work, the amount of these oxide phases is pretty low since the XRD peaks are very tiny and therefore we can infer that the ORR results are exclusively due to the presence of a large amount of Fe-N_X centers and N-pyridinic. Despite the outstanding achievements in alkaline media, the ORR performance provided by our electrocatalysts is far away from commercial PGMs and therefore these TM-N_x-Cs cannot fulfill the requirements of the acid fuel cell market. Since pyridinic is the most prominent nitrogen moiety, such disappointing results in acid might be mainly attributed to the protonation of pyridine rather than the poisoning effect of H_2SO_4 ions.[105,106] Among nitrogen moieties, pyridinic-N is the strongest basic group so it is more prone to protonation compared to the other nitrogen moieties.[107] The pKa of pyridinic-N is around 6 in doped graphene and therefore it becomes completely protonated in 0.5 M H_2SO_4.[106] This phenomenon decreases the charge density and basicity of adjacent carbon atoms and, in turn, this withdraws the electron density of the Fe center, thus leading to poor adsorption of oxygen and rapid demetallization of Fe-N_x sites.[99,107] Another adverse effect of pyridinic protonation is the higher production of hydrogen peroxide which is quite high (around 20%) for our electrocatalysts compared to other Fe-N_x-Cs synthesized in other works and containing a lower relative % of pyridinic sites.[108,109] In an alkaline environment, pyridinic-N is completely deprotonated, and therefore the previously described effects do not take place. In light of this, it can be stated that the greater the pyridinic content the more evident the difference in performance between the acid and alkaline environment.[106,107]

Conclusions

Following a circular economy approach, different components of cigarette butts, *i.e.* tobacco, filter and paper, and the entire extinguished cigarettes were utilized as carbon and nitrogen precursors to prepare Fe–N–C electrocatalysts. The obtained materials are amorphous with a high degree of defectivity provided by oxygen, nitrogen, and iron functionalities as well as oxide phases. Most of the elements occurring in small traces

within the initial precursor were completely absent in the final electrocatalysts due to the effectiveness of the acid washing used in the activation procedure. Even though the amount of N, Fe, and O was found to be different, the proportion of N, Fe, and O moieties is comparable among the electrocatalysts, thus giving rise to similar performance in the acid and alkaline media. The best results were achieved in an alkaline environment by ClGF_450 and ClGPF_450. They exhibit a $E_{1/2}$ of 0.89 V vs RHE and a slightly different E_{on}, *i.e.* 0.94 V vs RHE for ClGF_450 and 0.95 V vs RHE for ClGPF_450. The high performance of these electrocatalysts, comparable to those of Pt/C with 40 wt% of Pt in terms of activity but better in selectivity, and the high durability of the tested electrocatalyst, *i.e.* ClGF_450, are promising for alkaline fuel cell cathodes. These outstanding achievements are due to a high fraction of Fe-N_x and pyridinic-N, which, however, might negatively influence the acid performance due to its protonation. Last but not least, the work intends to show the effect of the cigarette components in the final electrochemical performance by following our synthetic procedure. Herein, no significant differences were detected, meaning that the cigarette component does not play a significant role in the electrochemical performance. Nevertheless, our outcome does not exclude that some differences might be observed by adopting another preparation procedure.

Experimental Section

Synthesis

Cigarette butts were collected from the ballot bins installed in the smoking area of the University of Milano-Bicocca Campus. After recovering, cigarette butts were air-dried overnight under a fume hood. Subsequently, the different components, *i.e.* paper, filter, and tobacco, were manually sorted from the used cigarettes. The different components, including whole cigarettes, were shredded by means of a coffee-grinding machine. Afterwards, the samples were pulverized via ball milling (Emax Retsch®) with stainless-steel balls and jars by setting 800 rpm as rotation speed, a processing time of 1 h divided into two intervals of 30 min processing, which were interrupted by 5 min of resting time. The as-obtained powder was poured into an alumina boat, which was placed at the center of a quartz tube of a tubular furnace (Naberthem®RSH 50/500/13). Before starting any heat treatment N_2 gas was flushed for *ca.* 30 min with a flow of 100 $cm^3 min^{-1}$ as to create an anoxic atmosphere. Afterward, the samples were pyrolyzed at 450 °C for 1 h with a rate of 5 °C min^{-1} upon constant N_2 flow. The as-obtained char was chemically activated with a KOH/carbon (4:1 w/w ratio). KOH was first dissolved in ethanol within. After the complete dissolution of KOH in ethanol, the char was added and the mixture was stirred at room temperature for a period of time between 12 and 24 h. Thereafter, the temperature was raised to 80 °C upon stirring, and constant nitrogen flux to allow the evaporation of the solvent under a dry atmosphere. The dried mixture was poured into an alumina boat covered with Ni strips to avoid reactions between aluminum oxide and the KOH embedded into the carbon at high temperatures. For a similar reason, the quartz tube employed for the activation was internally covered with a stainless-steel foil. After N_2 conditioning, the temperature was brought to 700 °C with a ramp of 5 °C min^{-1} and dwelled for 1 h upon a N_2 flux of 100 $cm^3 min^{-1}$. Afterwards, an acid washing with 1 M HCl was performed to remove KOH from the activated carbon and the acidic solution was repeatedly rinsed with milli-Q water under vacuum filtration until pH neutrality. Subsequently, the washed sample was dried all night in an oven. The functionalization was carried out by thoroughly mixing the activated char with 10 wt% of iron (II) phthalocyanine (FePc) and the obtained mixture was heat-treated at 600 °C for 1 h under N_2 flux of 100 $cm^3 min^{-1}$. The electrocatalysts derived from whole cigarette, filter, paper, and tobacco were respectively labeled as ClGF_450, ClGBF_450, ClGPF_450, and ClGTF_450.

Morphological and Chemical Characterizations

The surface morphology of the final materials was analyzed through a desktop scanning electron microscopy (SEM, Thermo Fisher Phenom G6, Eindhoven, Netherlands) equipped with a thermoionic CeB6 source. The secondary electron (SE) mode was adopted to acquire the sample images. TEM micrographs were obtained through Thermofisher Talos (F200X G2) equipped with a high-speed CETA camera. HAABF images were recorded using Panther annular STEM while the EDX mapping was performed with a Super X spectrometer attached with four 30 mm^2 silicon drift detectors having 0.7 srad collection angle.

The elemental analysis (CHNS) was performed using the Elementar Vario Microcube Device.

To study the carbonaceous structure, Raman spectroscopy (Jobin Yvon, France) was carried out. The instrumentation was composed of a helium-neon laser source (632.8 nm of wavelength), a microscope (BX40, Olympus, Japan) equipped with an objective lens of 50x magnification (0.6 N.A.) to focus the laser on the sample, and a silicon CCD detector working at 200 K to record the scattered signal (Sincerity, Jobin Yvon, France). The I_D/I_G ratio was calculated by using the absolute band intensity of D and G bands.

The qualitative inorganic elemental analysis was performed via X-rays fluorescence (XRF, Artax 200, Bruker, Billerica, MA, USA) possessing a Mo anode.

X-ray diffraction (XRD, Rigaku Miniflex 600, Tokyo, Japan) coupled with Cu source was used to study the crystallographic properties of the samples. The spectra were acquired in the window 10–80°. The BET-specific surface area was determined by nitrogen adsorption at 77 K using a Micromeritics ASAP 2020 analyzer. The samples were pretreated at 30 μmHg at 393.15 K for 15 h. The BET surface area was calculated in the pressure range between 0.1 and 0.22 p/p0 while the pore volume was calculated with the BJH method (17.00–3000.00 Å range).

The sample's chemical composition and speciation was investigated using X-ray Photoelectron Spectroscopy (XPS) in Ultra High Vacuum (UHV, $<10^{-9}$ mBar) using SPECS PHOIBOS 150 XPS system furnished with monochromatic Al K_α (1486.6 eV) X-ray source and high-speed imaging 2D CMOS true counting detector. The system was calibrated using Au4f spectra at 84 eV. The samples were prepared over a Molybdenum custom made sample holder. Upon the full survey scans, 4 different Core levels were identified C1s, O1s, N1s, Fe2p and analyzed with a passing energy set to 20 eV for all elements. The fittings were performed using Kalibri KolXPD software.

Electrochemical Characterization

The electrochemical measurements were carried out with rotating ring disk electrode (RRDE) technique. A Pine 250 mL glass cell was set up with a RRDE (Pine rotating electrode E6R2, USA), a saturated Ag/AgCl electrode and a graphite rod, serving as working, reference

and counter electrode, respectively. The electrodes were submerged in an 0.5 H_2SO_4 or 0.1 M KOH electrolyte. The electronics were controlled by Pine WaveDriver 200 EIS Bipotentiostat/Galvanostat (USA) and Pine WaveVortex 10 rotator (USA). The RRDE was made of concentric glassy carbon disk (0.2376 cm^2 geometric area) and Pt ring (0.2356 cm^2 geometric area). As a general rule, the RRDE was firstly polished with alumina paste on a cloth to obtain a flat surface. Meanwhile, the ink containing the electroactive material was prepared by suspending 5 mg of electrocatalyst in a mixture of 985 μL isopropanol (Alfa Aesar, Ward Hill, MA, USA) and 15 μL of 5 wt% Nafion®D-520 (Alfa Aesar, USA), and then sonicated with a probe sonicator for 10 min at 55% pulse amplitude. The as-prepared ink was drop-casted on the glassy carbon disk of RRDE with a loading of 0.6 mg cm^{-2}. Before running the measurements, the cell was bubbled with O_2 (99.9% purity) for 30 min. Subsequently, the electrocatalyst was cycled until signal stabilization at a scan rate of 100 mV s^{-1} within a potential window ranging between +1000 to −250 mV vs. Ag/AgCl (potential ring hold at 1000 mV vs. Ag/AgCl) in acid media and between +150 to −1050 mV vs. Ag/AgCl (potential ring hold at +150 mV vs. Ag/AgCl) in alkaline electrolyte. The step was carried out to activate the electrocatalyst. After that, a cyclic voltammetry was acquired at 50 mV s^{-1} to assess the presence of ORR activity in our electrocatalysts. Thereupon, linear sweep voltammetry (LSV) was acquired in the same potential window by setting a rotation speed of 1600 rpm and a scan rate of 5 mV s^{-1}. For the sake of comparison, the measured potentials were converted vs reverse hydrogen electrode (RHE) using the following equation: E(vs. RHE) = E(vs. Ag/AgCl) + 0.197 + 0.0591 pH. To correctly determine the faradaic current, the capacitive current must be subtracted by the LSV recorded in O_2 saturated electrolyte. Hence, all the LSV acquired in oxygen were subtracted by the LSV recorded in nitrogen saturated electrolyte (99.9% purity), as reported in other works. Moreover, all the measurements were corrected by iR drop compensation at 85%. The peroxide % and the number of transferred electrons were calculated according to the following equations:

$$Peroxide\ \% = \frac{200 \cdot \frac{J_{ring}}{N}}{J_{disk} + \frac{J_{ring}}{N}} \tag{4.1}$$

$$n = \frac{4J_{disk}}{J_{disk} + \frac{J_{ring}}{N}} \tag{4.2}$$

where J_{disk} and J_{ring} are the disk and ring current respectively while N is the collection efficiency, which is 0.38 according to the supplier. For the sake of comparison, a Pt/C (Alfa Aesar, 40 wt% of Pt) was drop-casted on RRDE with a loading of 30 $\mu g_{Pt}\,cm^{-2}$, which is the optimal loading suggested by previous reports.[110]

For the Tafel analysis, the kinetic current J_k was corrected by the limiting current J_{lim} according to this relationship:

$$J_k = \frac{J_{disk}J_{lim}}{J_{disk} - J_{lim}} \tag{4.3}$$

and the plot at low overpotential was carried out within the region between the E_{on} and the $E_{1/2}$.

An accelerated stability test (AST) of 2000 cycles was performed with the aforementioned RRDE setup and in the same potential window used for LSVs at 1600 rpm and 50 mV s^{-1} in O_2 saturated electrolyte. The catalyst loading was kept constant at 0.6 mg cm^{-2}. To compare the electrocatalyst state before and after AST, two LSVs were recorded at the 1st and the last cycle with a scan rate of 5 mV s^{-1}.

Acknowledgements

The cigarette butts fractionation has been performed within the MUSA – Multilayered Urban Sustainability Action – project, funded by the European Union – NextGenerationEU, under the National Recovery and Resilience Plan (NRRP) Mission 4 Component 2 Investment Line 1.5: Strengthening of research structures and creation of R&D "innovation ecosystems", set up of "territorial leaders in R&D".

G.Z. acknowledges a Ph.D. scholarship on the Italian National Ph.D. program "Scientific, technological and social methods enabling circular economy", Curriculum "Technical materials for circularity" funded by Italy's Recovery and Resilient Plan and EU Recovery Plan.

C.S. would like to thank the support from ENEA – UNIMIB agreement (Procedure 1.1.3 PNRR POR H2). C.S. would like to acknowledge also the Cariplo Foundation, Call for Circular Economy through the project "Transformation of plastic waste in Electrocatalysts, Supported by exhausted gases recovery Layout" (TESLA).

The integrated XPS were carried out at the SmartLab departmental laboratory of the Department of Physics at Sapienza University of Rome. EP and VCAF are grateful to Dr. M. Sbroscia for his assistance during the measurements. EP and VCAF acknowledge funding from the European Union - NextGenerationEU under the Italian Ministry of University and Research (MUR), \Network 4 Energy Sustainable Transition - NEST" project (MIUR project code PE000021, Concession Degree No. 1561 of October 11, 2022) – CUP C93C22005230007.

Conflict of Interests

The authors declare no conflict of interest.

Data Availability Statement

The data that support the findings of this study are available from the corresponding author upon reasonable request.

Keywords: cigarette butts · cigarette components · oxygen reduction reaction · PGM-free · Fe-N–C electrocatalysts

[1] A. Pramuanjaroenkij, S. Kakaç, *Int. J. Hydrogen Energy* **2023**, *48*, 9401–9425.
[2] E. Katz, P. Bollella, *Isr. J. Chem.* **2021**, *61*, 68–84.
[3] T. B. Ferriday, P. H. Middleton, *Int. J. Hydrogen Energy* **2021**, *46*, 18489–18510.
[4] A. T. Hamada, M. F. Orhan, A. M. Kannan, *Energy Reports* **2023**, *9*, 6396–6418.
[5] S. Mo, L. Du, Z. Huang, J. Chen, Y. Zhou, P. Wu, L. Meng, N. Wang, L. Xing, M. Zhao, Y. Yang, J. Tang, Y. Zou, S. Ye, *Electrochem. Energy Rev.* **2023**, *6*.

[6] N. Ramaswamy, S. Mukerjee, *Chem. Rev.* **2019**, *119*, 11945–11979.
[7] X. Ge, A. Sumboja, D. Wuu, T. An, B. Li, F. W. T. Goh, T. S. A. Hor, Y. Zong, Z. Liu, *ACS Catal.* **2015**, *5*, 4643–4667.
[8] E. Wallnöfer-Ogris, F. Poimer, R. Köll, M. G. Macherhammer, A. Trattner, *Int. J. Hydrogen Energy* **2023**.
[9] C. Santoro, A. Lavacchi, P. Mustarelli, V. Di Noto, L. Elbaz, D. R. Dekel, F. Jaouen, *ChemSusChem* **2022**, *15*.
[10] A. Sajid, E. Pervaiz, H. Ali, T. Noor, M. M. Baig, *Int. J. Energy Res.* **2022**, *46*, 6953–6988.
[11] L. Fan, H. Deng, Y. Zhang, Q. Du, D. Y. C. Leung, Y. Wang, K. Jiao, *Energy Environ. Sci.* **2023**, *16*, 1466–1479.
[12] J. Zhang, P. Xu, Z. Mao, X. Gao, E. Marquez, J. Y. Choi, Z. Chen, *J. Power Sources* **2023**, *586*.
[13] G. Daniel, T. Kosmala, M. C. Dalconi, L. Nodari, D. Badocco, P. Pastore, A. Lorenzetti, G. Granozzi, C. Durante, *Electrochim. Acta* **2020**, *362*, 137200.
[14] N. Zion, D. A. Cullen, P. Zelenay, L. Elbaz, *Angew. Chem.* **2020**, *132*, 2504–2510.
[15] S. Brocato, A. Serov, P. Atanassov, *Electrochim. Acta* **2013**, *87*, 361–365.
[16] M. M. Hossen, K. Artyushkova, P. Atanassov, A. Serov, *J. Power Sources* **2018**, *375*, 214–221.
[17] E. Proietti, F. Jaouen, M. Lefèvre, N. Larouche, J. Tian, J. Herranz, J. P. Dodelet, *Nat. Commun.* **2011**, *2*.
[18] S. Sun, J. Dang, K. Ji, Z. Shi, M. Chen, C. Zhang, S. Liu, *Renewable Sustainable Energy Rev.* **2023**, *183*.
[19] M. Muhyuddin, P. Mustarelli, C. Santoro, *ChemSusChem* **2021**, *14*, 3785–3800.
[20] S. S. Sekhon, J. Lee, J. S. Park, *J. Energy Chem.* **2021**, *65*, 149–172.
[21] V. Kumar, A. S. Vangnai, N. Sharma, K. Kaur, P. Chakraborty, M. Umesh, B. Singhal, D. Utreja, E. U. Carrasco, R. Andler, M. K. Awasthi, M. J. Taherzadeh, *Chemosphere* **2023**, *319*.
[22] S. Park, J. Song, W. C. Lee, S. Jang, J. Lee, J. Kim, H. K. Kim, K. Min, *Chem. Eng. J.* **2023**, *470*.
[23] Z. Chen, S. Yun, L. Wu, J. Zhang, X. Shi, W. Wei, Y. Liu, R. Zheng, N. Han, B. J. Ni, *Nano-Micro Lett.* **2023**, *15*.
[24] K. R. Vanapalli, H. B. Sharma, S. Anand, V. P. Ranjan, H. Singh, B. K. Dubey, B. Mohanty, *J. Hazard. Mater.* **2023**, *453*.
[25] G. Shah, U. Bhatt, V. Soni, *Heliyon* **2023**, *9*.
[26] M. C. B. Araújo, M. F. Costa, *Environ. Res.* **2019**, *172*, 137–149.
[27] F. Soleimani, S. Dobaradaran, G. E. De-la-Torre, T. C. Schmidt, R. Saeedi, *Sci. Total Environ.* **2022**, *813*.
[28] M. Shen, Y. Li, B. Song, C. Zhou, J. Gong, G. Zeng, *Sci. Total Environ.* **2021**, *791*.
[29] M. Conradi, J. E. Sánchez-Moyano, *Sci. Total Environ.* **2022**, *847*.
[30] T. Asset, P. Atanassov, *Joule* **2020**, *4*, 33–44.
[31] N. Zion, J. C. Douglin, D. A. Cullen, P. Zelenay, D. R. Dekel, L. Elbaz, *Adv. Funct. Mater.* **2021**, *31*.
[32] U. I. Kramm, J. Herranz, N. Larouche, T. M. Arruda, M. Lefèvre, F. Jaouen, P. Bogdanoff, S. Fiechter, I. Abs-Wurmbach, S. Mukerjee, J. P. Dodelet, *Phys. Chem. Chem. Phys.* **2012**, *14*, 11673–11688.
[33] K. Artyushkova, A. Serov, S. Rojas-Carbonell, P. Atanassov, *J. Phys. Chem. C* **2015**, *119*, 25917–25928.
[34] M. Skorupska, A. Ilnicka, J. P. Lukaszewicz, *Sci. Rep.* **2021**, *11*.
[35] K. Liu, J. Fu, Y. Lin, T. Luo, G. Ni, H. Li, Z. Lin, M. Liu, *Nat. Commun.* **2022**, *13*, DOI 10.1038/s41467-022-29797-1.
[36] M. Muhyuddin, J. Filippi, L. Zoia, S. Bonizzoni, R. Lorenzi, E. Berretti, L. Capozzoli, M. Bellini, C. Ferrara, A. Lavacchi, C. Santoro, *ChemSusChem* **2022**, *15*.
[37] M. Muhyuddin, D. Testa, R. Lorenzi, G. M. Vanacore, F. Poli, F. Soavi, S. Specchia, W. Giurlani, M. Innocenti, L. Rosi, C. Santoro, *Electrochim. Acta* **2022**, *433*, 141254.
[38] K. Liivand, J. Sainio, B. P. Wilson, I. Kruusenberg, M. Lundström, *Appl. Catal. B* **2023**, *332*.
[39] A. Veksha, K. Yin, J. G. S. Moo, W. Da Oh, A. Ahamed, W. Q. Chen, P. Weerachanchai, A. Giannis, G. Lisak, *J. Hazard. Mater.* **2020**, *387*.
[40] V. Sridhar, H. Park, *Materials* **2020**, *13*.
[41] M. Muhyuddin, N. Zocche, R. Lorenzi, C. Ferrara, F. Poli, F. Soavi, C. Santoro, *Mater. Renew. Sustain. Energy* **2022**, *11*, 131–141.
[42] S. Zago, M. Bartoli, M. Muhyuddin, G. M. Vanacore, P. Jagdale, A. Tagliaferro, C. Santoro, S. Specchia, *Electrochim. Acta* **2022**, *412*, 140128.
[43] Y. Fang, H. Wang, H. Yu, F. Peng, *Electrochim. Acta* **2016**, *213*, 273–282.
[44] S. A. Mirshokraee, M. Muhyuddin, R. Morina, L. Poggini, E. Berretti, M. Bellini, A. Lavacchi, C. Ferrara, C. Santoro, *J. Power Sources* **2023**, *557*, 232571.
[45] H. S. Kim, J. Lee, J. H. Jang, H. Jin, V. K. Paidi, S. H. Lee, K. S. Lee, P. Kim, S. J. Yoo, *Appl. Surf. Sci.* **2021**, *563*.
[46] S. A. Mirshokraee, M. Muhyuddin, R. Lorenzi, G. Tseberlidis, C. Lo Vecchio, V. Baglio, E. Berretti, A. Lavacchi, C. Santoro, *SusMat* **2023**, *3*, 248–262.
[47] J. Wei, Y. Liang, Y. Hu, B. Kong, G. P. Simon, J. Zhang, S. P. Jiang, H. Wang, *Angew. Chem.* **2016**, *128*, 1377–1381.
[48] D. Testa, G. Zuccante, M. Muhyuddin, R. Landone, A. Scommegna, R. Lorenzi, M. Acciarri, E. Petri, F. Soavi, L. Poggini, L. Capozzoli, A. Lavacchi, N. Lamanna, A. Franzetti, L. Zoia, C. Santoro, *Catalysts* **2023**, *13*.
[49] A. De Fenzo, M. Giordano, L. Sansone, *Materials* **2020**, *13*.
[50] J. Puls, S. A. Wilson, D. Hölter, *J. Polym. Environ.* **2011**, *19*, 152–165.
[51] J. Shen, J. Li, X. Qian, W. Ren, P. Fatehi, *Carbohydr. Polym.* **2014**, *101*, 769–775.
[52] S. Yousef, J. Eimontas, N. Striūgas, M. Praspaliauskas, M. A. Abdelnaby, *Biomass Convers. Biorefin.* **2022**.
[53] X. Tong, J. Hou, Y. Li, H. Li, W. Wu, Y. Guo, Y. Liu, D. Fu, X. Huang, Z. Xiong, J. Jiang, L. Qi, H. Wang, W. Cai, *Int. J. Hydrogen Energy* **2022**, *47*, 22972–22980.
[54] M. Liang, W. Lu, P. Lei, L. Wang, B. Wang, B. Li, Y. Shen, K. Zhang, *Waste Biomass Valorization* **2020**, *11*, 6369–6382.
[55] Y. F. Wu, Y. C. Hsiao, Y. J. Ou, S. Kubendhiran, C. Y. Huang, S. Yougbaré, L. Y. Lin, *J. Energy Storage* **2022**, *54*.
[56] G. P. Kim, M. Lee, H. D. Song, S. Bae, J. Yi, *Catal. Commun.* **2016**, *78*, 1–6.
[57] C. Yu, H. Hou, X. Liu, L. Han, Y. Yao, Z. Dai, D. Li, *Front. Mater.* **2018**, *5*.
[58] B. Janković, M. Kojić, M. Milošević, M. Rosić, H. Waisi, B. Božilović, N. Manić, V. Dodevski, *Polymers (Basel).* **2023**, *15*.
[59] D. Zhao, Y. Dai, K. Chen, Y. Sun, F. Yang, K. Chen, *J. Anal. Appl. Pyrolysis* **2013**, *102*, 114–123.
[60] C. Luo, D. Li, L. Huang, Z. Wang, J. Zhang, H. Liu, Z. Liu, *RSC Adv.* **2021**, *11*, 1662–1667.
[61] C. P. da Silva, T. E. de Almeida, R. Zittel, T. R. de Oliveira Stremel, C. E. Domingues, J. Kordiak, S. X. de Campos, *Environ. Monit. Assess.* **2016**, *188*.
[62] V. Gridin, J. Du, S. Haller, P. Theis, K. Hofmann, G. K. H. Wiberg, U. I. Kramm, M. Arenz, *Electrochim. Acta* **2023**, *444*.
[63] A. Ferrari, J. Robertson, *Phys. Rev. B: Condens. Matter Mater. Phys.* **2000**, *61*, 14095–14107.
[64] A. C. Ferrari, D. M. Basko, *Nature Publishing Group* **2013**, *8*, 235–246.
[65] Z. Li, L. Deng, I. A. Kinloch, R. J. Young, *Prog. Mater. Sci.* **2023**, *135*.
[66] A. Sadezky, *Carbon* **2005**, *43*, 1731–1742.
[67] Z. Li, L. Deng, I. A. Kinloch, R. J. Young, *Prog. Mater. Sci.* **2023**, *135*.
[68] C. Tang, Q. Zhang, *Adv. Mater.* **2017**, *29*.
[69] J. Zhu, S. Mu, *Adv. Funct. Mater.* **2020**, *30*.
[70] W. da S. Freitas, A. D'Epifanio, V. C. A. Ficca, E. Placidi, F. Arciprete, B. Mecheri, *Electrochim. Acta* **2021**, *391*.
[71] B. Mecheri, V. C. A. Ficca, M. A. Costa de Oliveira, A. D'Epifanio, E. Placidi, F. Arciprete, S. Licoccia, *Appl. Catal. B* **2018**, *237*, 699–707.
[72] W. da Silva Freitas, B. Mecheri, C. Lo Vecchio, I. Gatto, V. Baglio, V. C. A. Ficca, A. Patra, E. Placidi, A. D'Epifanio, *J. Power Sources* **2022**, *550*.
[73] V. C. A. Ficca, C. Santoro, E. Placidi, F. Arciprete, A. Serov, P. Atanassov, B. Mecheri, *ACS Catal.* **2023**, *13*, 2162–2175.
[74] W. da Silva Freitas, A. D'Epifanio, C. Lo Vecchio, I. Gatto, V. Baglio, V. C. A. Ficca, E. Placidi, B. Mecheri, *Chem. Eng. J.* **2023**, *465*.
[75] B. Ricciardi, B. Mecheri, W. da Silva Freitas, V. C. A. Ficca, E. Placidi, I. Gatto, A. Carbone, A. Capasso, A. D'Epifanio, *ChemElectroChem* **2023**, *10*.
[76] M. Jerigová, M. Odziomek, N. López-Salas, *ACS Omega* **2022**, *7*, 11544–11554.
[77] Y. Chen, Y. Huang, M. Xu, T. Asset, X. Yan, K. Artyushkova, M. Kodali, E. Murphy, A. Ly, X. Pan, I. V. Zenyuk, P. Atanassov, *Mater. Today* **2022**, *53*, 58–70.
[78] V. P. Vasiliev, R. A. Manzhos, V. K. Kochergin, A. G. Krivenko, E. N. Kabachkov, A. V. Kulikov, Y. M. Shulga, G. L. Gutsev, *Materials* **2022**, *15*.
[79] S. Kabir, K. Artyushkova, A. Serov, P. Atanassov, *ACS Appl. Mater. Interfaces* **2018**, *10*, 11623–11632.
[80] S. M. Unni, S. Devulapally, N. Karjule, S. Kurungot, *J. Mater. Chem.* **2012**, *22*, 23506–23513.
[81] J. Quílez-Bermejo, E. Morallón, D. Cazorla-Amorós, *Carbon* **2020**, *165*, 434–454.
[82] Z. Liu, Z. Zhao, Y. Wang, S. Dou, D. Yan, D. Liu, Z. Xia, S. Wang, *Adv. Mater.* **2017**, *29*.

[83] N. Chubar, V. Gerda, M. Szlachta, G. Yablokova, *Solid State Sci.* **2021**, *121*.
[84] A. P. Grosvenor, B. A. Kobe, M. C. Biesinger, N. S. McIntyre, *Surf. Interface Anal.* **2004**, *36*, 1564–1574.
[85] W. Sudarsono, S. Y. Tan, W. Y. Wong, F. S. Omar, K. Ramya, S. Mehmood, A. Numan, R. Walvekar, M. Khalid, *J. Ind. Eng. Chem.* **2023**, *122*, 1–26.
[86] K. Shinozaki, B. S. Pivovar, S. S. Kocha, S. Jayabal, G. Saranya, D. Geng, L. Y. Lin, X. Meng, S. S. Kocha, K. Shinozaki, J. W. Zack, D. J. Myers, N. N. Kariuki, T. Nowicki, V. Stamenkovic, Y. Kang, D. Li, D. Papageorgopoulos, *J. Mater. Chem. A Mater.* **2017**, *8*, 15–26.
[87] N. Ramaswamy, U. Tylus, Q. Jia, S. Mukerjee, *J. Am. Chem. Soc.* **2013**, *135*, 15443–15449.
[88] P. C. Okonkwo, I. Ben Belgacem, W. Emori, P. C. Uzoma, *Int. J. Hydrogen Energy* **2021**, *46*, 27956–27973.
[89] Y. He, G. Wu, *Acc. Mater. Res.* **2022**, *3*, 224–236.
[90] D. Banham, S. Ye, K. Pei, J. I. Ozaki, T. Kishimoto, Y. Imashiro, *J. Power Sources* **2015**, *285*, 334–348.
[91] M. A. C. de Oliveira, V. C. A. Ficca, R. Gokhale, C. Santoro, B. Mecheri, A. D'Epifanio, S. Licoccia, P. Atanassov, *Journal of Solid State Electrochemistry* **2021**, *25*, 93–104.
[92] K. Singh, F. Razmjooei, J. S. Yu, *J. Mater. Chem. A Mater.* **2017**, *5*, 20095–20119.
[93] V. Yarlagadda, M. K. Carpenter, T. E. Moylan, R. S. Kukreja, R. Koestner, W. Gu, L. Thompson, A. Kongkanand, *ACS Energy Lett.* **2018**, *3*, 618–621.
[94] X. Han, T. Zhang, X. Wang, Z. Zhang, Y. Li, Y. Qin, B. Wang, A. Han, J. Liu, *Nat. Commun.* **2022**, *13*.
[95] N. Ramaswamy, S. Mukerjee, *Adv. Phys. Chem.* **2012**, *2012*, 1–17.
[96] H. S. Park, E. Seo, J. Yang, Y. Lee, B. S. Kim, H. K. Song, *Sci. Rep.* **2017**, *7*.
[97] Z. L. Wang, D. Xu, H. X. Zhong, J. Wang, F. L. Meng, X. B. Zhang, *Sci. Adv.* **2015**, *1*.
[98] X. Li, C. S. Cao, S. F. Hung, Y. R. Lu, W. Cai, A. I. Rykov, S. Miao, S. Xi, H. Yang, Z. Hu, J. Wang, J. Zhao, E. E. Alp, W. Xu, T. S. Chan, H. Chen, Q. Xiong, H. Xiao, Y. Huang, J. Li, T. Zhang, B. Liu, *Chem.* **2020**, *6*, 3440–3454.
[99] Q. Ma, H. Jin, J. Zhu, Z. Li, H. Xu, B. Liu, Z. Zhang, J. Ma, S. Mu, *Adv. Sci.* **2021**, *8*.
[100] C. H. Choi, C. Baldizzone, J. Grote, A. K. Schuppert, F. Jaouen, K. J. J. Mayrhofer, *Angew. Chem.* **2015**, *127*, 12944–12948.
[101] Y. P. Ku, K. Ehelebe, A. Hutzler, M. Bierling, T. Böhm, A. Zitolo, M. Vorokhta, N. Bibent, F. D. Speck, D. Seeberger, I. Khalakhan, K. J. J. Mayrhofer, S. Thiele, F. Jaouen, S. Cherevko, *J. Am. Chem. Soc.* **2022**, *144*, 9753–9763.
[102] R. Gokhale, Y. Chen, A. Serov, K. Artyushkova, P. Atanassov, *Electrochem. Commun.* **2016**, *72*, 140–143.
[103] K. Xu, H. Bao, C. Tang, K. Maliutina, F. Li, L. Fan, *Mater. Today Energy* **2020**, *18*.
[104] R. Sgarbi, K. Kumar, V. A. Saveleva, L. Dubau, R. Chattot, V. Martin, M. Mermoux, P. Bordet, P. Glatzel, E. A. Ticianelli, F. Jaouen, F. Maillard, *Appl. Catal. B* **2022**, *311*.
[105] W. Orellana, C. Zuñiga, A. Gatica, M. S. Ureta-Zanartu, J. H. Zagal, F. Tasca, *ACS Catal.* **2022**, *12*, 12786–12799.
[106] M. Rauf, Y. Di Zhao, Y. C. Wang, Y. P. Zheng, C. Chen, X. D. Yang, Z. Y. Zhou, S. G. Sun, *Electrochem. Commun.* **2016**, *73*, 71–74.
[107] H. Y. Wang, C. C. Weng, Z. Y. Yuan, *J. Energy Chem.* **2021**, *56*, 470–485.
[108] Y. Chen, R. Gokhale, A. Serov, K. Artyushkova, P. Atanassov, *Nano Energy* **2017**, *38*, 201–209.
[109] M. Primbs, Y. Sun, A. Roy, D. Malko, A. Mehmood, M. T. Sougrati, P. Y. Blanchard, G. Granozzi, T. Kosmala, G. Daniel, P. Atanassov, J. Sharman, C. Durante, A. Kucernak, D. Jones, F. Jaouen, P. Strasser, *Energy Environ. Sci.* **2020**, *13*, 2480–2500.
[110] Y. Garsany, O. A. Baturina, K. E. Swider-Lyons, S. S. Kocha, *Anal. Chem.* **2010**, *82*, 6321–6328.

Manuscript received: November 29, 2023
Revised manuscript received: February 23, 2024
Version of record online: April 30, 2024